




Article

Dependence of Photocatalytic Activity on the Morphology of Strontium Titanates

Tamás Gyulavári ^{1,*} , Daniella Dusnoki ¹, Viktória Márta ¹, Mohit Yadav ¹, Mahsa Abedi ¹, András Sági ¹ , Ákos Kukovecz ¹, Zoltán Kónya ¹  and Zsolt Pap ^{1,2,3,*}

¹ Department of Applied and Environmental Chemistry, University of Szeged, Rerrich Béla Sqr. 1, H-6720 Szeged, Hungary; d.daniella0226@gmail.com (D.D.); martaviktoria95@gmail.com (V.M.); yadavmohit27@gmail.com (M.Y.); mahsa.sh.abedi@gmail.com (M.A.); sapia@chem.u-szeged.hu (A.S.); kakos@chem.u-szeged.hu (Á.K.); konya@chem.u-szeged.hu (Z.K.)

² Nanostructured Materials and Bio-Nano-Interfaces Center, Interdisciplinary Research Institute on Bio-Nano-Sciences, Babes-Bolyai University, Treboniu Laurian 42, RO-400271 Cluj-Napoca, Romania

³ Institute of Research-Development-Innovation in Applied Natural Sciences, Babes-Bolyai University, Fântânele Str. 30, RO-400294 Cluj-Napoca, Romania

* Correspondence: gyulavarit@chem.u-szeged.hu (T.G.); pzsolt@chem.u-szeged.hu (Z.P.); Tel.: +36-62-544-626 (T.G.); +36-62-543-795 (Z.P.)

Abstract: Strontium titanates were prepared with different morphologies by varying the ratio of solvents used during the synthesis. The effects of morphology and solvent (ethylene glycol to water) ratio were investigated both on the structure and photocatalytic activity of the samples. Structural properties were determined by X-ray diffraction, scanning electron microscopy, diffuse reflectance spectroscopy, and nitrogen adsorption measurements. The photocatalytic activity of the samples was evaluated by the photocatalytic oxidation of phenol and by the photocatalytic reduction of carbon dioxide. The ratio of solvents notably influenced the morphology, strontium carbonate content, primary crystallite size, and specific surface area of the samples. Samples prepared at low ethylene glycol to water ratios were spherical, while the ones prepared at high ethylene glycol to water ratios could be characterized predominantly by lamellar morphology. The former samples were found to have the highest efficiency for phenol degradation, while the sample with the most well-defined lamellar morphology proved to be the best for CO₂ reduction.

Keywords: strontium titanate; morphology; water treatment; phenol; CO₂ reduction; photocatalysis



Citation: Gyulavári, T.; Dusnoki, D.; Márta, V.; Yadav, M.; Abedi, M.; Sági, A.; Kukovecz, Á.; Kónya, Z.; Pap, Z. Dependence of Photocatalytic Activity on the Morphology of Strontium Titanates. *Catalysts* **2022**, *12*, 523. <https://doi.org/10.3390/catal12050523>

Academic Editor: Roberto Fiorenza

Received: 18 March 2022

Accepted: 27 April 2022

Published: 7 May 2022

Publisher's Note: MDPI stays neutral with regard to jurisdictional claims in published maps and institutional affiliations.



Copyright: © 2022 by the authors. Licensee MDPI, Basel, Switzerland. This article is an open access article distributed under the terms and conditions of the Creative Commons Attribution (CC BY) license (<https://creativecommons.org/licenses/by/4.0/>).

1. Introduction

For photocatalytic applications, strontium titanate (SrTiO₃) can have numerous benefits in comparison with conventional binary oxides such as TiO₂. The conduction band edge of the former is approximately 200 mV more negative than that of the latter [1], making it more suitable for photocatalytic reduction. Strontium ions in SrTiO₃ can facilitate the formation of superoxide radicals and inhibit the recombination of photogenerated charge carriers which is conducive for photocatalytic oxidation [2]. Many attempts have been made to increase the photocatalytic activity of SrTiO₃ photocatalysts via methods such as doping [3–6], metal deposition [7–10], and morphological modifications [9–12].

Morphological modifications include changing properties such as the size, specific surface area (SSA), shape, and porosity of photocatalysts [1], all of which can influence photocatalytic activity. For example, small primary crystallite sizes usually result in large SSAs, more accessible crystallographic planes, and reduced recombination of charge carriers in the bulk [13]. Certain crystallographic planes within the same material can be photocatalytically more active than others. For instance, Chen et al. found that for BiVO₄, the sample possessing the highest relative intensity ratio of the (040) and (−121) crystallographic planes proved to be the best for the degradation of methylene blue [14]. Kedves et al. found that

the photocatalytic activity of α - MoO_3 increased with increasing (040) facet ratio compared with that of the (110) or (021) facets [15]. Bárdos et al. reported that the dominance of the (102) crystallographic plane in BiOCl materials resulted in a redshift in the band gap energy, thus, influencing photocatalytic activity [16]. Moreover, the preparation of shape-controlled nanocrystals is a frequently applied approach to enhance photocatalytic activity. Balázs et al. highlighted that in heterogeneous catalytic processes, catalytic activity and the density of catalytically active sites are influenced by crystal faces, thus, by the shape of catalyst crystals [17]. They reported that samples containing predominantly polyhedral crystals possessed superior photocatalytic activity for phenol degradation compared with that of samples containing spherical crystals. Conversely, when Wahi et al. investigated the photocatalytic activity of nanospheres and nanorods for Congo red decomposition, they found that nanospheres (nanodots) had better photoactivity [18]. They attributed the poor photoactivity of nanorods to the non-dissociative adsorption of water to shapes with such morphology, resulting in hindered $\bullet\text{OH}$ generation. Xu et al. prepared needle-, cube-, granule-, and plate-like crystals and investigated the effect of morphology on the photoactivity for methyl orange degradation [19]. They found that needle-shaped photocatalysts had the best photocatalytic activity and attributed this to their highest SSA. Xiang et al. compared the effect of various spherical morphologies (spheres, hollow spheres, porous spheres, urchin-like spheres) on the photocatalytic activity in their review [20]. They highlighted porous spheres to be highly efficient due to the pores serving as a light-transfer path, enabling the incident photon flux to reach the interior surface and more light waves to be captured. On a similar note, in our earlier publication, we found TiO_2 hollow spheres to be highly efficient for the degradation of phenol [21]. We attributed this to the better utilization of incident light waves due to them constructively interfering with each other. As for SrTiO_3 -based photocatalysts, there are many publications in the literature where they have been synthesized in cubic [12,22–24], spherical [9,11], star/flower-like [9], and urchin-like [7,9] shapes. In publications where photocatalytic degradation efficiency was investigated, organic dyes were used as pollutants in most cases [3,4,7,11,12,24].

In this study, SrTiO_3 photocatalysts were fabricated with different morphologies. The influence of morphology on photocatalytic activity was investigated in detail. To the best of our knowledge, the number of publications systematically investigating the dependence of photooxidation activity on morphology is scarce, especially for pollutants other than organic dyes. Consequently, phenol was used in this paper to study the photooxidation activity of SrTiO_3 photocatalysts. Their photoreduction activity was also investigated in relation to morphology via the photocatalytic reduction of CO_2 .

2. Results and Discussion

2.1. Characterization

2.1.1. XRD, N_2 Adsorption, and DRS Measurements

The X-ray diffraction (XRD) patterns at 22.7° , 32.3° , 39.9° , 46.5° , 57.7° , and 67.7° 2θ degrees (Figure 1) were attributed to the (100), (110), (111), (200), (211), and (220) crystallographic planes of SrTiO_3 (JCPDS 35-0734), respectively [25]. The reflections at 25.1° , 25.7° , 29.1° , 36.5° , and 44.1° could be ascribed to the (111), (021), (002), (130), and (132) crystallographic planes of SrCO_3 (JCPDS 05-0418), respectively [26]. In the following paragraphs, we investigated those structural features that can influence the photocatalytic activity according to the literature.

First, we investigated the effect of ethylene glycol to water (EG: H_2O) ratio on the primary crystallite size of the samples. The numbers in each sample name correspond to the ratio of EG to H_2O . The intensity of the XRD patterns decreased with increasing EG: H_2O ratios indicating that the crystallinities and primary crystallite sizes were decreased. The latter was calculated using the Scherrer equation and the results are summarized in Table 1. EG notably inhibited the growth of crystals until reaching the EG: H_2O ratio of 2:1; however, above this ratio only small changes were observed. Based on the publication of Xu et al.

lower EG:H₂O ratio (i.e., higher water content) can facilitate nucleation, but the adsorption of EG inhibits the growth of crystal seeds at the same time [27].

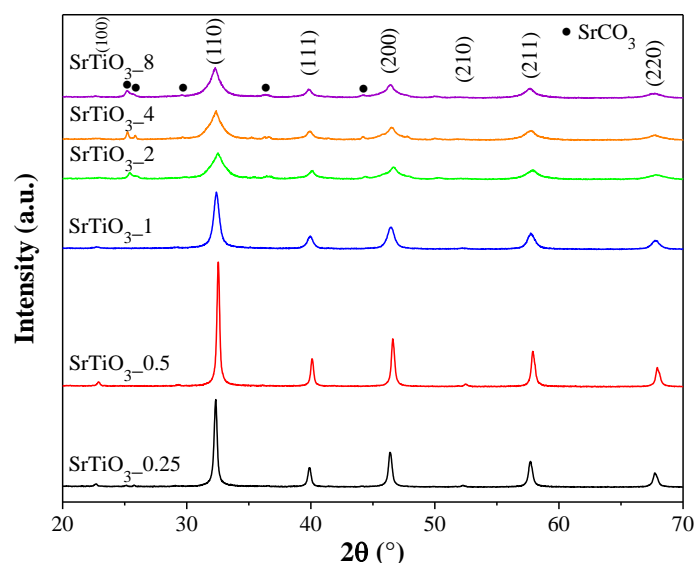


Figure 1. XRD patterns of SrTiO₃ photocatalysts prepared at various EG:H₂O ratios.

Table 1. Dependence of structural properties, optical properties, photocatalytic activity, and methane production on the EG:H₂O ratios applied during the synthesis of SrTiO₃ photocatalysts.

Sample Name	Size (nm)	Specific Surface Area (m ² ·g ⁻¹)	SrCO ₃ Content (%)	$I_{(111)/(110)}$	Band Gap (eV)	$r_{0,phenol}$ (10 ⁻⁹ M·s ⁻¹)	TOR _{s,phenol} (μmol/m ² /h)	r_{0,CO_2} (10 ⁻¹¹ mol·s ⁻¹)	TOR _{s,CO_2} (μmol/m ² /h)	CH ₄ Selectivity (%)
SrTiO ₃ _0.25	30.6	26	1.23	0.22	3.29	1.46	2.0×10^{-2}	9.35	1.3×10^{-2}	1.99
SrTiO ₃ _0.5	32.9	14	0.29	0.21	3.28	1.34	3.5×10^{-2}	7.66	2.0×10^{-2}	3.99
SrTiO ₃ _1	17.2	55	0.18	0.24	3.34	0.99	6.5×10^{-3}	10.17	6.7×10^{-3}	3.52
SrTiO ₃ _2	8.4	146	3.53	0.27	3.33	1.01	2.5×10^{-3}	8.49	2.1×10^{-3}	4.76
SrTiO ₃ _4	9.8	123	4.62	0.25	3.34	1.20	3.5×10^{-3}	8.86	2.6×10^{-3}	4.64
SrTiO ₃ _8	10.5	117	10.94	0.26	3.36	1.20	3.7×10^{-3}	9.97	3.1×10^{-3}	3.72

Second, we investigated the changes in the intensity ratios of the (111) and (110) crystallographic planes ($I_{(111)/(110)}$). Based on the publication of Zhao et al., the presence of the former has a beneficial effect on the photocatalytic activity [28]. With the increase of the EG:H₂O ratio, the ratio of this crystallographic plane also increased predominantly (Table 1).

Third, we investigated the SSA of the samples via N₂ adsorption using the Brunauer–Emmett–Teller (BET) method. Similar to our findings on primary crystallite size vs solvent ratio, no regular trend was observed in the change of SSAs (Table 1). However, it can be ascertained that small EG:H₂O ratios predominantly resulted in large primary crystallite sizes and small SSAs, and vice versa. Consequently, the results of the N₂ adsorption measurements and Scherrer calculations were in good accordance with each other: with increasing particle sizes the SSAs decreased.

Fourth, we investigated the dependence of SrCO₃ content on the EG:H₂O ratio. It was established that with increasing EG:H₂O ratio, SrCO₃ content predominantly increased as well (Table 1). The increase of SSA with EG:H₂O ratio was deduced to be responsible for this finding. The appearance of SrCO₃ in the samples can be ascribed to the presence of CO₂ in the air [1]. This causes the appearance of CO₃²⁻ ions in the synthesis mixture which can react with Sr²⁺ ions, resulting in SrCO₃ [24]. Another source of CO₃²⁻ ions could be the NaOH used during the synthesis. NaOH contains a small amount of Na₂CO₃ impurity, and it can easily capture CO₂ from the air. The presence of SrCO₃ can be beneficial for the photocatalytic activity [29,30]. It can enhance the separation of photogenerated charge

carriers since the valence band of SrCO_3 can accept electrons from the valence band of SrTiO_3 [31].

Fifth, the diffuse reflectance spectra (DRS) of the samples were recorded and considered. The results were shown by plotting both the absorbance (Figure 2a) and the first order derivative of reflectance values (Figure 2b) as a function of wavelength. The band gaps were between 3.28 and 3.36 eV, which are reasonably close to the most frequently reported value of 3.2 eV [1]. However, based on the first derivative spectra, another set of electron transition bands were also observed varying between 3.62 and 3.8 eV values. Based on the literature, these can also be attributed to SrTiO_3 in the form of thin films [32] or single crystals [33]. However, considering that NaOH was used during the synthesis of the samples, the formation of Na_2TiO_3 is also probable. This assumption is supported both by our previous publication [34] and by the publication of Bastida et al. [35]. In both studies, the formation of Na_2TiO_3 was observed in the same region as in the present work. In summary, the samples prepared in this work had very similar band gaps; thus, variations in their photocatalytic activities, presumably, will not be attributable to these differences.

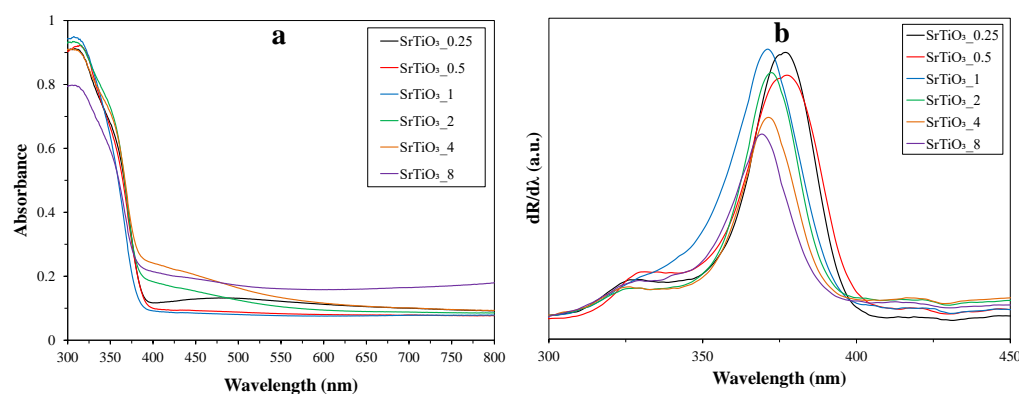


Figure 2. DR (a) absorbance and (b) first order derivative spectra of SrTiO_3 photocatalysts prepared at various EG:H₂O ratios.

2.1.2. SEM Measurements

The results of scanning electron microscopy (SEM) measurements are shown in Figure 3. $\text{SrTiO}_3_{0.25}$ (Figure 3a) and $\text{SrTiO}_3_{0.5}$ (Figure 3b) had spherical morphology (with average diameters of ~186 and 871 nm, respectively). It is well known that the shape of a sphere has the lowest possible surface area to volume ratio. This fact is in good accordance with our findings, as these two samples had the lowest SSA values and, accordingly, the highest surface-normalized photocatalytic activities (Section 2.2, Table 1). SrTiO_3_{1} (Figure 3c) had rather well-defined lamellar morphology (denoted as “star-like” morphology by Zhou et al. [9]). So far, these results were in good accordance with their publication. In contrast, SrTiO_3_{2} , SrTiO_3_{4} , and SrTiO_3_{8} (Figure 3d–f, respectively) could not be characterized with well-defined morphologies. However, generally, increasing the EG:H₂O ratio during the synthesis resulted in the formation of lamellar morphology (well observable for SrTiO_3_{1} and SrTiO_3_{4} in particular), but the trend was not regular. It is known that EG can inhibit crystal growth, because it can adsorb on the surface of particles, thus, blocking possible growth directions. Moreover, EG can stabilize the newly formed crystals as well [36]. Consequently, EG can take a significant part in tailoring the morphology of crystals, as it was observed in our case as well. Zhou et al. also attributed the formation of various morphologies to the presence of EG [9]. They reported that a film was formed on the surface of SrTiO_3 nanoparticles due to hydrogen bonding and hydrophobic interactions. This influenced crystal growth, resulting in various morphologies.

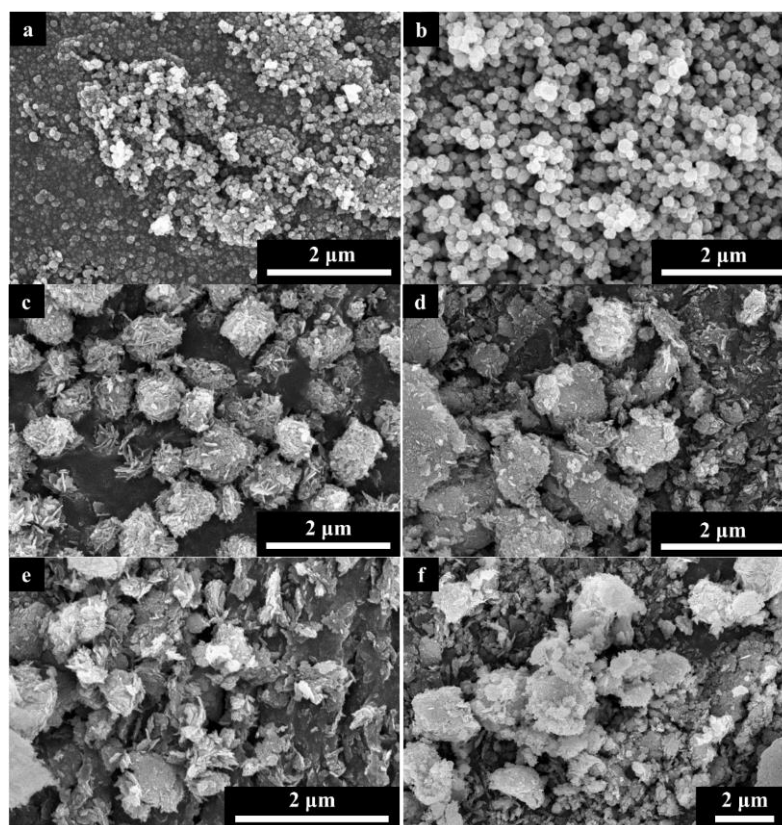


Figure 3. SEM micrographs of SrTiO₃ photocatalysts prepared at (a) 0.25, (b) 0.5, (c) 1, (d) 2, (e) 4, and (f) 8 EG:H₂O ratios.

2.2. Photocatalytic Activity Measurements

2.2.1. Photocatalytic Oxidation of Phenol

The photocatalytic activity of the samples was evaluated via the photocatalytic oxidation of phenol, and the results are summarized in Figure 4 and Table 1. The changes in the concentration of phenol measured at the beginning and end of the adsorption/desorption equilibrium tests were below 1%. This was within the range of error of our high-performance liquid chromatograph (HPLC). To ensure the reliability of results, the tests were carried out for SrTiO₃_0.5 two additional times and the difference in conversion values were less than 0.55% (Figure S1). In the absence of photocatalysts (“Blank”), no degradation occurred. Commercial reference SrTiO₃ (“SrTiO₃_ref”) degraded only a negligible amount of phenol (conversion: ~1.5%). Our samples proved to be significantly better (conversion: ~12–15%); however, the differences in conversion values were less than 3.5%. Hence, to better evaluate the results, initial degradation rates and surface normalized turnover rates (TOR_s) were calculated. These values were summarized and collated with the properties, mentioned above, that influence photocatalytic activity (i.e., SSA, SrCO₃ content, EG:H₂O ratio, $I_{(111)/(110)}$ /morphology).

It was found that spherical SrTiO₃_0.25 and SrTiO₃_0.5 had both the best absolute and surface normalized photocatalytic activities. Since the degradation of phenol is a radical-mediated process, the SSAs did not have a major effect on the conversion values, as expected. Based on the publication of Fodor et al., commercial Sigma Aldrich anatase and Aeroxide P25 titania have comparable photocatalytic activities for phenol degradation despite the notable difference in their SSAs [37]. For the fact that SSA did not notably influence photocatalytic activity, another explanation could be the following: after the excitation of semiconductors, the charge carriers formed as a result (electron–hole pairs) can be separated by interparticle charge transfer, as the electrons move within the bulk crystal. The larger the particles, the higher the number is of those electrons that can travel

across the bulk of the material [38]. This can result in enhanced charge separation (a phenomenon which is exploited in the fabrication of photoanodes [39]) and, as such, enhanced photoactivity. There were notable differences in the SrCO₃ content of the samples, yet this property did not affect their photocatalytic activity. This was rather unexpected since, based on the literature, the presence of SrCO₃ is usually beneficial for both photocatalytic oxidation [31,40] and photocatalytic CO₂ reduction [29,30]. Last, with the increase of EG:H₂O ratio, the dominance of the (111) crystallographic plane increased, but both the absolute and surface normalized photocatalytic activities decreased predominantly, contrary to expectations.

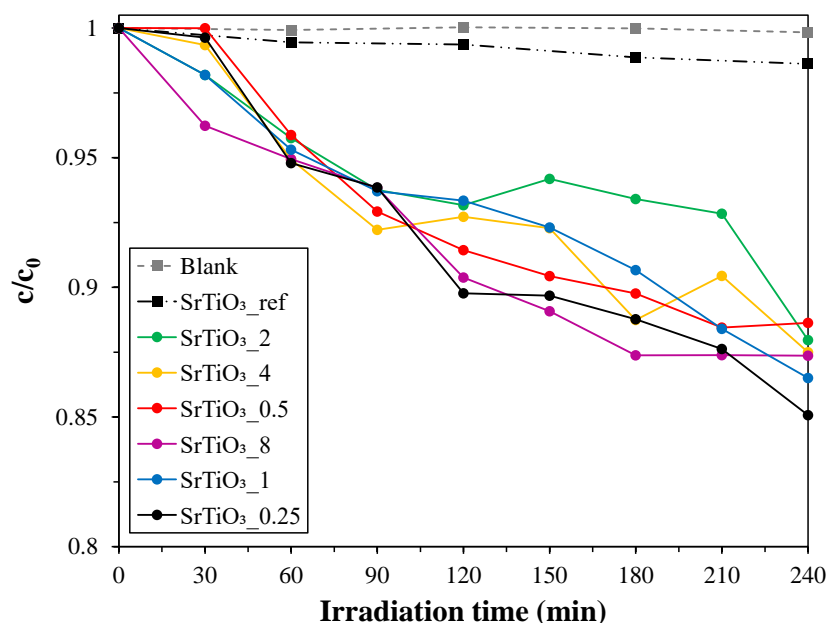


Figure 4. Degradation curves of phenol for SrTiO₃ photocatalysts prepared at various EG:H₂O ratios.

2.2.2. Photocatalytic Reduction of CO₂

The photocatalytic activity of the samples was evaluated via the photocatalytic reduction of CO₂ as well, and the results are summarized in Figure 5 and Table 1. Same as for phenol, the reliability of results was checked via carrying out the tests for SrTiO_{3_0.5} two additional times, and the difference in conversion values were less than 0.2% (Figure S2). No conversion occurred in the absence of photocatalysts, as was the case for phenol. A conversion of ~13% was observed for SrTiO_{3_ref}, which was poorer than that for any of our own samples. The differences in conversion values were rather small once again (less than 2.8%); therefore, the same steps were taken as in Section 2.2.1. It was found that SrTiO_{3_1} and SrTiO_{3_8} had the best absolute photocatalytic activity; however, SrTiO_{3_0.25} and SrTiO_{3_0.5} still had the best surface normalized photoactivity due to their low SSAs.

Based on all of these results, it was ascertained that the parameters associated with morphology (and SrCO₃ content) did not significantly influence photocatalytic activity for these materials in these reactions. Thus, it was deduced that all of the crystallographic planes must be accessible to the formation of charge carriers. It is also worth highlighting that SrTiO_{3_1} had the best absolute photocatalytic activity and the most well-defined lamellar morphology. If we only consider the samples prepared at higher EG:H₂O ratios (i.e., SrTiO_{3_1}, SrTiO_{3_2}, SrTiO_{3_4}, SrTiO_{3_8}) possessing lamellar morphology then, out of these samples, SrTiO_{3_1} possessed the highest surface normalized photocatalytic activity as well. Thus, the possible effects of lamellar morphology were investigated more thoroughly. Nakagava et al. found lamellar titanate nanosheets to be significantly more efficient for Rhodamine B degradation than commercial reference P25 TiO₂ [41]. They attributed this difference to the finding that lamellar structures could adsorb cationic organic compounds better through cation exchange. They also highlighted that this morphology enables

the intercalation of water molecules via hydrogen bonding, facilitating the separation of electron–hole pairs, leading to better photoactivity. Yao et al. prepared lamellar β - In_2S_3 photocatalysts and investigated their efficiency for methyl orange degradation in comparison with non-lamellar β - In_2S_3 [42]. The sample possessing the most well-defined lamellar morphology proved to be the best, and the authors attributed this to its highest SSA. Chen et al. prepared a series of BiVO_4 photocatalysts using EG and H_2O as solvents, and investigated the effect of solvent ratio on the properties of the samples [14]. They found the solvent ratio to influence numerous properties of the photocatalysts, similar to our findings in the present paper: intensity ratios of crystallographic planes, band gap values, morphology, and photocatalytic activity. As in our case, solvent ratio did not significantly influence band gap values; however, it had a profound effect on the morphology. They found that the sample possessing lamellar morphology and the highest $I_{(040)}/I_{(-121)}$ ratio to be the most efficient for methylene blue degradation in comparison with samples with other morphologies. They attributed this to the lowest band gap and the more efficient separation of electron–hole pairs. Similar to the findings in these publications, in the present paper the sample with the most well-defined lamellar morphology (SrTiO_3 _1) had the best photocatalytic activity for CO_2 conversion. This could be due to SrTiO_3 _1 having an extended electron transition band at 335–350 nm, which is absent from the other samples. This can result in the better excitation of SrTiO_3 _1 in this wavelength interval.

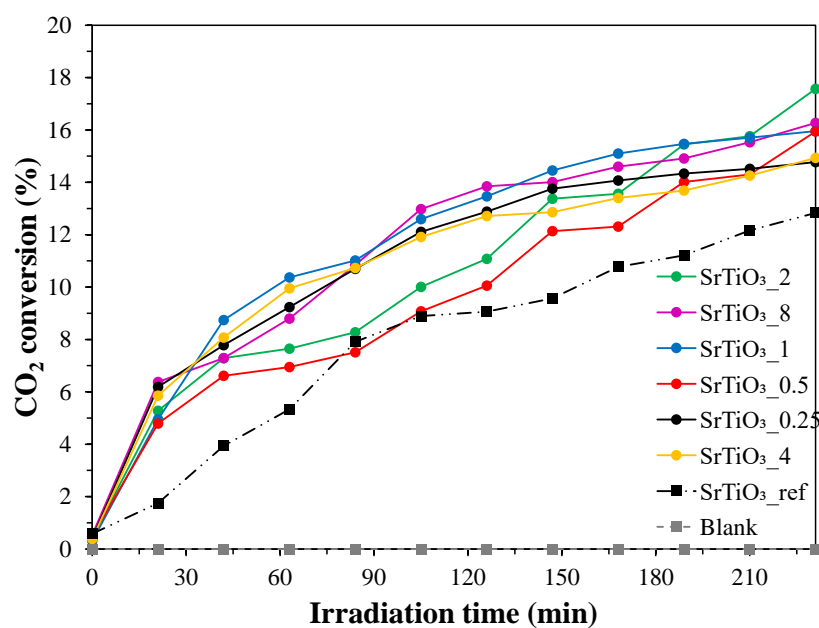
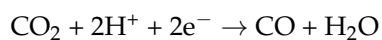
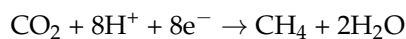


Figure 5. Photocatalytic conversion of CO_2 with SrTiO_3 photocatalysts prepared at various EG: H_2O ratios.

During the photocatalytic reduction of CO_2 (in the presence of H_2), two products were identified: predominantly, carbon monoxide was produced, but the formation of 1.99–4.76% methane was also observed (Table 1). After comparing the CH_4 selectivities and surface normalized CO_2 conversion rates it was found that, in most cases, with the increase of the former, the latter decreased. This may indicate that the formation of methane takes place in multiple steps, or that more charge carriers are required for this process than for the conversion of CO_2 to CO . The latter assumption is supported by the following chemical equations [43]:



Finally, photocatalytic activity results of the present study were compared with other ones from the literature for reference, which were summarized in Table S1.

3. Materials and Methods

3.1. Materials

Strontium nitrate (Molar Chemicals, Halásztelek, Hungary; 98.5%) and titanium (IV) butoxide (Sigma-Aldrich, Schnellendorf, Germany; reagent grade, 97%) were used as SrTiO₃ precursors. Ethylene glycol (VWR Chemicals, Debrecen, Hungary; Reag. Ph. Eur.) and ultrapure Millipore Milli-Q water (Budapest, Hungary) were used as solvents. Sodium hydroxide (Molar Chemicals, Halásztelek, Hungary; >97%) was used to set an alkaline environment. Ethanol (Molar Chemicals, Halásztelek, Hungary; absolute ethanol) and Milli-Q water were used to purify the samples via centrifugation. Phenol (Spektrum 3D, Debrecen, Hungary; analytical grade) and a gas mixture of CO₂:H₂ = 1:2 ratio were used for the photocatalytic activity measurements. Commercial SrTiO₃ (Alfa Aesar, Kandel, Germany; 99%) was used as a reference photocatalyst.

3.2. Synthesis

The synthesis procedure was based on the publication of Zhou et al. [9]. SrTiO₃ photocatalysts with different morphologies were synthesized solvothermally by varying the volume ratios of the solvents (Table 2). Accordingly, titanium (IV) butoxide was added to EG under vigorous magnetic stirring. After 10 min, 5 M sodium hydroxide solution was added, which was followed by the dropwise addition of 0.5 M strontium nitrate solution. The mixture was stirred for 1 h, transferred to a Teflon[®]-lined stainless steel autoclave (Toption, Xi'an, China; V_{total} = 150 mL), and heat treated at 180 °C for 24 h. Then, it was allowed to cool down to room temperature. After collecting the samples, we purified them by centrifugation in four cycles (two times with absolute ethanol and two times with Milli-Q water for 5 min per cycle at 4400 rpm). Finally, the samples were dried overnight and ground in an agate mortar. The names of the samples and the volumes of the reactants used during the synthesis are summarized in Table 2.

Table 2. Volumes of reactants and EG:H₂O ratios applied during the synthesis of SrTiO₃ photocatalysts.

Sample Name	EG (mL)	Ti(IV) Butoxide (mL)	NaOH (mL)	Sr(NO ₃) ₂ (mL)	H ₂ O (mL)	EG:H ₂ O Ratio
SrTiO ₃ _0.25	18.3	8.3	24.5	48.9	73.4	0.25
SrTiO ₃ _0.5	30.0	6.8	20.0	40.0	60.0	0.5
SrTiO ₃ _1	47.1	5.3	15.7	31.4	47.1	1.0
SrTiO ₃ _2	63.0	3.6	10.5	21.0	31.5	2.0
SrTiO ₃ _4	78.0	2.2	6.5	13.0	19.5	4.0
SrTiO ₃ _8	87.6	1.2	3.7	7.3	11.0	8.0

3.3. Characterization Methods and Instrumentation

To determine the crystalline composition of the samples, we carried out XRD measurements with a Rigaku Miniflex II diffractometer (Rigaku, Neu-Isenburg, Germany) using the following parameters: $\lambda_{\text{Cu K}\alpha} = 0.15406$ nm, 30 mA and 40 kV, 20–70 (2 θ) region. SrCO₃ content of the samples was calculated by dividing the peak area of the most intense diffraction corresponding to SrCO₃ by the peak area of the most intense diffraction corresponding to SrTiO₃. To investigate the morphology of the samples, we took SEM measurements with a Hitachi S-4700 Type II microscope (Hitachi, Tokyo, Japan) applying 10 kV acceleration voltage. To calculate the SSA of the samples, we performed nitrogen adsorption measurements with a BELCAT-A device (Microtrac MRB, Osaka, Japan) and used the BET method. To investigate optical properties, we recorded the DR spectra of the samples with a Jasco-V650 spectrophotometer (Jasco, Tokyo, Japan) equipped with an ILV-724-type integration sphere. The band gap energies were calculated from the first order derivative spectra of the samples.

3.4. Photocatalytic Activity Measurements

The photooxidation activity of the samples was evaluated by using phenol as a pollutant ($c = 0.1$ mM). The catalysts ($m = 100$ mg) were put in beakers and suspended in 100 mL of phenol-containing water. The photocatalyst suspensions were stirred in the dark for 30 min to reach adsorption/desorption equilibrium. The samples were excited with three UV fluorescent tubes (Lighttech, Dunakeszi, Hungary; UV-A, $\lambda_{\max} = 355$ nm, 40 W) that were placed above the beakers (irradiation height = 15 cm). During these 4-hour-long measurements, constant magnetic stirring was provided. The concentration of phenol was measured with a high-performance liquid chromatograph (HPLC). The device applied was an Agilent 1290 Infinity II (Santa Clara, CA, USA) that consisted of a binary pump and a diode array detector ($\lambda_{\text{detection}} = 210$ nm). A Poroshell 120 C18 column was used as the stationary phase, containing particles with a diameter of 2.7 μm . As eluent, an 80:20 (v/v) mixture of methanol and water was used with a flow rate of 1 $\text{mL}\cdot\text{min}^{-1}$.

The photoreduction activity of the samples was investigated via the photocatalytic hydrogenation of CO_2 . For this purpose, a flow microreactor was assembled that consisted of an inner ($d_{\text{inner}} = 6.4$ cm, $h = 25$ cm) and an outer glass cylinder ($d_{\text{inner}} = 10.2$ cm, $h = 25$ cm). The smaller glass cylinder contained a 500 W mercury vapor lamp (Heraeus Noblelight TQ 718, Hanau, Germany; $\lambda_{\max} = 254$ nm) as a light source that was operated under constant water cooling. First, 250 mg of catalyst was suspended in 10 mL of absolute ethanol via ultrasonication, which was then immobilized on the outer surface of the smaller glass cylinder. Second, the inner cylinder was heated to 250 $^{\circ}\text{C}$, with a heating rod, while various gases were introduced into the space between the cylinders (Ar for 20 min, O_2 for 30 min, Ar for 10 min, and H_2 for 60 min in this order) to pretreat the immobilized catalysts. Third, the gas mixture containing CO_2/H_2 at a ratio of 1:2 was introduced into the space between the cylinders with an Aalborg mass flow controller (Hazel Park, MI, USA). A pump was used to recirculate the fixed amount of CO_2/H_2 gas mixture between the reactor and gas chromatograph (GC). During the measurements, a constant (room) temperature was set by recirculating cooling water through the system. Fourth, the products were introduced into a HP 5890 Series II GC for analysis. The separation of the reactants and products was carried out via a 2-meter-long ($d = 0.635$ cm) capillary column packed with a Porapak QS polymer (Bellefonte, PA, USA). The gases were detected with a thermal conductivity detector and a flame ionization detector.

Photocatalytic activity data was expressed as surface normalized turnover rate (TOR_s), as well for better comparability based on the publication of Wachs et al. [44].

4. Conclusions

SrTiO_3 photocatalysts with different morphologies were successfully prepared by varying the EG: H_2O ratio applied during the synthesis. Primary crystallite sizes increased with the EG content until the 2:1 ratio, then no significant change occurred. SrCO_3 content and the dominance of the (111) crystallographic plane increased with increasing EG content in most cases. Overall, small EG: H_2O ratios predominantly resulted in large primary crystallite sizes, small SSAs, and spherical morphology, while large EG: H_2O ratios resulted in small primary crystallite sizes, high SSAs, and predominantly lamellar morphology.

The samples prepared in this work proved to be significantly better both for phenol degradation and CO_2 conversion than commercial reference SrTiO_3 . The SrCO_3 content of the samples did not notably affect their photoactivity. Their SSAs did not significantly influence phenol degradation efficiency since it is a radical-mediated process. As the dominance of the (111) crystallographic plane increased, the rate of phenol degradation decreased. The SrTiO_3 sample possessing the most well-defined lamellar morphology was found to be the best for CO_2 conversion (both in terms of absolute and relative photoactivity). This was mainly attributed to this sample having an extended electron transition band at 335–350 nm that could result in its better excitability in this wavelength interval. CO was the main product of CO_2 reduction, but methane was also generated to a lesser extent (1.99–4.76%). With the increase of CH_4 selectivity, the surface normalized

CO₂ conversion rates decreased. This finding was attributed to the different number of electrons required to convert CO₂ either to CO or to CH₄.

Supplementary Materials: The following supporting information can be downloaded at: <https://www.mdpi.com/article/10.3390/catal12050523/s1>, Figure S1: Degradation curves of phenol repeated two times using SrTiO₃_0.5, Figure S2: Photocatalytic conversion of CO₂ repeated two times using SrTiO₃_0.5. Table S1: Comparison of photocatalytic activity results of the present study with other ones from the literature [44–49].

Author Contributions: T.G.: conceptualization, supervision, funding acquisition, writing—original draft, writing—review and editing; D.D.: conceptualization, investigation; V.M.: investigation; Z.K.: conceptualization; M.Y.: investigation; M.A.: investigation; A.S.: supervision; Á.K.: resources; Z.K.: resources; and Z.P.: conceptualization, supervision, funding acquisition. All authors have read and agreed to the published version of the manuscript.

Funding: This study was financed by the 2019-2.1.13-TÉT_IN-2020-00015 project. T. Gyulavári is grateful for the financial support of the NKFI-PD-138248 project. Z. Pap acknowledges the Bolyai János scholarship provided by the Hungarian Academy of Sciences. Project no. TKP2021-NVA-19 has been implemented with the support provided by the Ministry of Innovation and Technology of Hungary from the National Research, Development, and Innovation Fund, financed under the TKP2021-NVA funding scheme.

Data Availability Statement: Data is contained within the article or Supplementary Material.

Conflicts of Interest: The authors declare no conflict of interest.

References

1. Phoon, B.L.; Lai, C.W.; Juan, J.C.; Show, P.L.; Chen, W.H. A review of synthesis and morphology of SrTiO₃ for energy and other applications. *Int. J. Energy Res.* **2019**, *43*, 5151–5174. [[CrossRef](#)]
2. Yousefi, R.; Jamali-Sheini, F.; Cheraghizade, M.; Khosravi-Gandomani, S.; SÁaedi, A.; Huang, N.M.; Basirun, W.J.; Azarang, M. Enhanced visible-light photocatalytic activity of strontium-doped zinc oxide nanoparticles. *Mater. Sci. Semicond. Process.* **2015**, *32*, 152–159. [[CrossRef](#)]
3. Xu, J.; Wei, Y.; Huang, Y.; Wang, J.; Zheng, X.; Sun, Z.; Fan, L.; Wu, J. Solvothermal synthesis nitrogen doped SrTiO₃ with high visible light photocatalytic activity. *Ceram. Int.* **2014**, *40*, 10583–10591. [[CrossRef](#)]
4. Gao, X.; Li, M.; Zhou, F.; Wang, X.; Chen, S.; Yu, J. Flexible zirconium doped strontium titanate nanofibrous membranes with enhanced visible-light photocatalytic performance and antibacterial activities. *J. Colloid Interface Sci.* **2021**, *600*, 127–137. [[CrossRef](#)]
5. Sukpanish, P.; Lertpanyapornchai, B.; Yokoi, T.; Ngamcharussrivichai, C. Lanthanum-doped mesostructured strontium titanates synthesized via sol-gel combustion route using citric acid as complexing agent. *Mater. Chem. Phys.* **2016**, *181*, 422–431. [[CrossRef](#)]
6. Kiss, B.; Manning, T.D.; Hesp, D.; Didier, C.; Taylor, A.; Pickup, D.M.; Chadwick, A.V.; Allison, H.E.; Dhanak, V.R.; Claridge, J.B.; et al. Nano-structured rhodium doped SrTiO₃–Visible light activated photocatalyst for water decontamination. *Appl. Catal. B Environ.* **2017**, *206*, 547–555. [[CrossRef](#)]
7. Shi, L.; Zhang, Z.; Wang, R.; Zhou, C.; Sun, C. Synthesis and post-annealing of Ag nanoparticles decorated urchin-like SrTiO₃ particles for enhanced electron/hole separation and photocatalytic activity. *Ceram. Int.* **2020**, *46*, 19460–19468. [[CrossRef](#)]
8. Taşyürek, L.B.; Aydoğlan, Ş.; Sevim, M.; Çaldıran, Z. Synthesis of nickel nanoparticles-deposited strontium titanate nanocubes (Ni-STO) and heterojunction electrical applications over a wide temperature range. *Mater. Sci. Eng. B* **2021**, *274*, 115479. [[CrossRef](#)]
9. Zhou, M.; Chen, J.; Zhang, Y.; Jiang, M.; Xu, S.; Liang, Q.; Li, Z. Shape-controlled synthesis of golf-like, star-like, urchin-like and flower-like SrTiO₃ for highly efficient photocatalytic degradation and H₂ production. *J. Alloy. Compd.* **2020**, *817*, 152796. [[CrossRef](#)]
10. Kuang, Q.; Yang, S. Template synthesis of single-crystal-like porous SrTiO₃ nanocube assemblies and their enhanced photocatalytic hydrogen evolution. *ACS Appl. Mater. Interfaces* **2013**, *5*, 3683–3690. [[CrossRef](#)]
11. Dong, W.; Li, X.; Yu, J.; Guo, W.; Li, B.; Tan, L.; Li, C.; Shi, J.; Wang, G. Porous SrTiO₃ spheres with enhanced photocatalytic performance. *Mater. Lett.* **2012**, *67*, 131–134. [[CrossRef](#)]
12. Liu, Y.; Qian, Q.; Li, J.; Zhu, X.; Zhang, M.; Zhang, T. Photocatalytic Properties of SrTiO₃ Nanocubes Synthesized Through Molten Salt Modified Pechini Route. *J. Nanosci. Nanotechnol.* **2016**, *16*, 12321–12325. [[CrossRef](#)]
13. Hernández-Alonso, M.D.; Fresno, F.; Suárez, S.; Coronado, J.M. Development of alternative photocatalysts to TiO₂: Challenges and opportunities. *Energy Environ. Sci.* **2009**, *2*, 1231. [[CrossRef](#)]
14. Chen, L.; Wang, J.; Meng, D.; Xing, Y.; Wang, C.; Li, F.; Wang, Y.; Wu, X. Enhanced photocatalytic activity of hierarchically structured BiVO₄ oriented along {040} facets with different morphologies. *Mater. Lett.* **2015**, *147*, 1–3. [[CrossRef](#)]
15. Kedves, E.-Z.; Bárdos, E.; Gyulavári, T.; Pap, Z.; Hernadi, K.; Baia, L. Dependence of cationic dyes' adsorption upon α-MoO₃ structural properties. *Appl. Surf. Sci.* **2022**, *573*, 151584. [[CrossRef](#)]

16. Bardos, E.; Marta, V.A.; Fodor, S.; Kedves, E.Z.; Hernadi, K.; Pap, Z. Hydrothermal Crystallization of Bismuth Oxychlorides (BiOCl) Using Different Shape Control Reagents. *Materials* **2021**, *14*, 2261. [[CrossRef](#)]
17. Balázs, N.; Mogyorósi, K.; Srankó, D.F.; Pallagi, A.; Alapi, T.; Oszkó, A.; Dombi, A.; Sipos, P. The effect of particle shape on the activity of nanocrystalline TiO₂ photocatalysts in phenol decomposition. *Appl. Catal. B Environ.* **2008**, *84*, 356–362. [[CrossRef](#)]
18. Wahi, R.K.; Yu, W.W.; Liu, Y.; Mejia, M.L.; Falkner, J.C.; Nolte, W.; Colvin, V.L. Photodegradation of Congo Red catalyzed by nanosized TiO₂. *J. Mol. Catal. A Chem.* **2005**, *242*, 48–56. [[CrossRef](#)]
19. Xu, H.-Y.; Li, B.; Li, P. Morphology dependent photocatalytic efficacy of zinc ferrite probed for methyl orange degradation. *J. Serb. Chem. Soc.* **2018**, *83*, 1261–1271. [[CrossRef](#)]
20. Xiang, L.; Zhao, X. Wet-Chemical Preparation of TiO₂-Based Composites with Different Morphologies and Photocatalytic Properties. *Nanomaterials* **2017**, *7*, 310. [[CrossRef](#)]
21. Gyulavári, T.; Kovács, K.; Kovács, Z.; Bárdos, E.; Kovács, G.; Baán, K.; Magyari, K.; Veréb, G.; Pap, Z.; Hernadi, K. Preparation and characterization of noble metal modified titanium dioxide hollow spheres—New insights concerning the light trapping efficiency. *Appl. Surf. Sci.* **2020**, *534*, 147327. [[CrossRef](#)]
22. Gao, H.; Yang, H.; Wang, S. Hydrothermal synthesis, growth mechanism, optical properties and photocatalytic activity of cubic SrTiO₃ particles for the degradation of cationic and anionic dyes. *Optik* **2018**, *175*, 237–249. [[CrossRef](#)]
23. Ramos-Sanchez, J.E.; Camposeco, R.; Lee, S.-W.; Rodriguez-González, V. Sustainable synthesis of AgNPs/strontium-titanate-perovskite-like catalysts for the photocatalytic production of hydrogen. *Catal. Today* **2020**, *341*, 112–119. [[CrossRef](#)]
24. Huang, S.-T.; Lee, W.W.; Chang, J.-L.; Huang, W.-S.; Chou, S.-Y.; Chen, C.-C. Hydrothermal synthesis of SrTiO₃ nanocubes: Characterization, photocatalytic activities, and degradation pathway. *J. Taiwan Inst. Chem. Eng.* **2014**, *45*, 1927–1936. [[CrossRef](#)]
25. Le, M.-V.; Vo, N.-Q.-D.; Le, Q.-C.; Tran, V.A.; Phan, T.-Q.-P.; Huang, C.-W.; Nguyen, V.-H. Manipulating the Structure and Characterization of Sr_{1-x}La_xTiO₃ Nanocubes toward the Photodegradation of 2-Naphthol under Artificial Solar Light. *Catalysts* **2021**, *11*, 564. [[CrossRef](#)]
26. Asgari-Fard, Z.; Sabet, M.; Salavati-Niasari, M. Synthesis and Characterization of Strontium Carbonate Nanostructures via Simple Hydrothermal Method. *High. Temp. Mater. Processes* **2016**, *35*, 215–220. [[CrossRef](#)]
27. Xu, G.; Huang, X.; Zhang, Y.; Deng, S.; Wei, X.; Shen, G.; Han, G. Self-assembly and formation mechanism of single-crystal SrTiO₃ nanosheets via solvothermal route with ethylene glycol as reaction medium. *CrystEngComm* **2013**, *15*, 7206. [[CrossRef](#)]
28. Zhao, H.; Fan, Z.; Fu, Q.; Wang, H.; Hu, Z.; Tao, H.; Zhang, X.; Ma, Z.; Jia, T. Enhanced photocatalytic performance of SrTiO₃ crystals with (100), (110) and (111) orientations treated by N₂ (H₂) plasma. *J. Mater. Sci.* **2018**, *53*, 15340–15347. [[CrossRef](#)]
29. Jin, J.; Chen, S.; Wang, J.; Chen, C.; Peng, T. SrCO₃-modified brookite/anatase TiO₂ heterophase junctions with enhanced activity and selectivity of CO₂ photoreduction to CH₄. *Appl. Surf. Sci.* **2019**, *476*, 937–947. [[CrossRef](#)]
30. Li-Mei, G.U.O.; Yuan-Jiang, K.; Xiao-Dan, Y.; Yan-Long, Y.U.; Jiang-Hong, Y.A.O.; Ya-An, C.A.O. Investigation on Photocatalytic Reduction of CO₂ into CH₄ Using SrB₂O₄/SrCO₃ Composite Catalyst. *Acta Phys.-Chim. Sin.* **2013**, *29*, 1558–1565. [[CrossRef](#)]
31. Jin, S.; Dong, G.; Luo, J.; Ma, F.; Wang, C. Improved photocatalytic NO removal activity of SrTiO₃ by using SrCO₃ as a new co-catalyst. *Appl. Catal. B Environ.* **2018**, *227*, 24–34. [[CrossRef](#)]
32. Weiss, C.V.; Zhang, J.; Spies, M.; Abdallah, L.S.; Zollner, S.; Cole, M.W.; Alpay, S.P. Bulk-like dielectric properties from metallo-organic solution-deposited SrTiO₃ films on Pt-coated Si substrates. *J. Appl. Phys.* **2012**, *111*, 054108. [[CrossRef](#)]
33. Trepakov, V.; Dejneka, A.; Markovin, P.; Lynnyk, A.; Jastrabik, L. A ‘soft electronic band’ and the negative thermo-optic effect in strontium titanate. *New J. Phys.* **2009**, *11*, 083024. [[CrossRef](#)]
34. Gyulavári, T.; Veréb, G.; Pap, Z.; Dombi, A.; Hernádi, K. Associating low crystallinity with peroxy groups for enhanced visible light active photocatalysts. *Catal. Today* **2018**, *313*, 231–238. [[CrossRef](#)]
35. Bastida, M.A.C.; Maldonado, Y.G.; Vidal, Y.R.; Lopez, M.S.; Gonzalez, E.C.; Ayala, F.E. Sodium Titanate Synthesis for the Photocatalytic Degradation of NO. *Res. Sq.* **2021**. [[CrossRef](#)]
36. Hai, C.; Li, S.; Zhou, Y.; Zeng, J.; Ren, X.; Li, X. Roles of ethylene glycol solvent and polymers in preparing uniformly distributed MgO nanoparticles. *J. Asian Ceram. Soc.* **2018**, *5*, 176–182. [[CrossRef](#)]
37. Fodor, S.; Kovács, G.; Hernádi, K.; Danciu, V.; Baia, L.; Pap, Z. Shape tailored Pd nanoparticles’ effect on the photocatalytic activity of commercial TiO₂. *Catal. Today* **2017**, *284*, 137–145. [[CrossRef](#)]
38. Lowekamp, J.B.; Rohrer, G.S.; Morris Hotsenpiller, P.A.; Bolt, J.D.; Farneth, W.E. Anisotropic Photochemical Reactivity of Bulk TiO₂ Crystals. *J. Phys. Chem. B* **1998**, *102*, 7323–7327. [[CrossRef](#)]
39. Yu, Z.; Chen, L.; Luo, L.; Huang, R.; Tang, Z.; Xiao, P.; Zhang, Y. Combining Bulk Charge Transport and Surface Charge Transfer to Design Titanium-Doped Hematite Homo Junction Photoanodes. *J. Phys. Chem. C* **2022**, *126*, 4296–4305. [[CrossRef](#)]
40. Parambil, J.A.; Mujeeb, A.V.M.; Parayil, S.K. P123 assisted sol-gel combustion synthesis of mesoporous strontium titanate nanomaterials for photocatalytic degradation of methylene blue. *Indian J. Chem. A-Inorgh. Bio-Inorgh. Phys. Theor. Anal. Chem.* **2021**, *60*, 1443–1451.
41. Nakagawa, K.; Yamaguchi, K.; Yamada, K.; Sotowa, K.I.; Sugiyama, S.; Adachi, M. Synthesis and Characterization of Surface-Functionalized Layered Titanate Nanosheets Using Lamellar Self-Assembly as a Template. *Eur. J. Inorgh. Chem.* **2012**, *2012*, 2741–2748. [[CrossRef](#)]
42. Yao, W.; Chen, Y.; Li, J.; Yang, J.; Ren, S.; Liu, W.; Liu, Q. Photocatalytic degradation of methyl orange by Ca doped β-In₂S₃ with varying Ca concentration. *Res. Chem. Intermed.* **2022**, *48*, 1813–1829. [[CrossRef](#)]

43. Chang, X.; Wang, T.; Gong, J. CO₂ photo-reduction: Insights into CO₂ activation and reaction on surfaces of photocatalysts. *Energy Environ. Sci.* **2016**, *9*, 2177–2196. [[CrossRef](#)]
44. Wachs, I.E.; Phivilay, S.P.; Roberts, C.A. Reporting of Reactivity for Heterogeneous Photocatalysis. *ACS Catal.* **2013**, *3*, 2606–2611. [[CrossRef](#)]
45. Ahuja, S.; Kutty, T.R.N. Nanoparticles of SrTiO₃ prepared by gel to crystallite conversion and their photocatalytic activity in the mineralization of phenol. *J. Photochem. Photobiol. A* **1996**, *97*, 99–107. [[CrossRef](#)]
46. Grabowska, E.; Marchelek, M.; Klimczuk, T.; Lisowski, W.; Zaleska-Medynska, A. TiO₂/SrTiO₃ and SrTiO₃ microspheres decorated with Rh, Ru or Pt nanoparticles: Highly UV-vis responsible photoactivity and mechanism. *J. Catal.* **2017**, *350*, 159–173. [[CrossRef](#)]
47. Bi, Y.; Ehsan, M.F.; Huang, Y.; Jin, J.; He, T. Synthesis of Cr-doped SrTiO₃ photocatalyst and its application in visible-light-driven transformation of CO₂ into CH₄. *J. CO₂ Util.* **2015**, *12*, 43–48. [[CrossRef](#)]
48. Luo, C.; Zhao, J.; Li, Y.; Zhao, W.; Zeng, Y.; Wang, C. Photocatalytic CO₂ reduction over SrTiO₃: Correlation between surface structure and activity. *Appl. Surf. Sci.* **2018**, *447*, 627–635. [[CrossRef](#)]
49. Li, C.; Liu, Z.; Zhou, H.; Haminhgoc; Zhu, F.; Guo, Q.; Zhao, Z. Molten Salt Synthesis of SrTiO₃ Using TiO₂ with Different Morphology as a Precursor. *Integr. Ferroelectr.* **2015**, *162*, 113–121. [[CrossRef](#)]